An Enhanced Modular Multilevel Converter With Multiple MVAC Ports Based on Active Fundamental-Frequency Circulating Current Injection to Realize Full-Range Operation

Junxian Chen, Jianwen Zhang, *Senior Member, IEEE*, Jianqiao Zhou, *Member, IEEE*, Gang Shi, *Member, IEEE*, Yajun Jia, Han Wang, and Xu Cai, *Senior Member, IEEE*

***Abstract*—The extensive integration of new sources and loads threatens the safe operation of the conventional ac distribution networks. The soft normally open point (SNOP) is proposed as an efficient solution. However, the mainstream back-to-back modular multilevel converter (MMC) scheme requires numerous devices and capacitances, which is not conducive to popularization. Lately, a novel modular multilevel converter with multiple MVac ports (MACP-MMC) has been introduced, offering a significant reduction in the construction cost and volume. Nonetheless, the MACP-MMC has some application limitations: when the MMC's ac output current is minimal, the MACP-MMC's power balanced control submodule has insufficient ability to maintain the internal energy balance, leading to its failed operation. To address this issue, this manuscript presents an enhanced MACP-MMC (eMACP-MMC) that features wide adjustment range. The proposed eMACP-MMC improves the connection structure between the MMC part and the multiport interconnection module part with small cost, thus offering an extra energy exchange path with the circulating current. On the one hand, eMACP-MMC can work as "MACP-MMC mode" under the joint supply or consumption scenario. On the other hand, the internal energy balance can be achieved by actively injecting fundamental-frequency circulating current under the flexible interconnection scenario. Consequently, the eMACP-MMC is suitable for all the application scenario of SNOP. Meanwhile, the circulating current's other degree of freedom is used for eliminate the imbalance between the MMC's arms caused by the former component. Additionally, considering the shortcomings caused by circulating current, the eMACP-MMC's redundant degrees of freedom are used to minimize the injected circulating current. Then, the novel operating principle and the control strategy of eMACP-MMC are researched.**

***Index Terms*—Energy balance, modular multilevel converter, multiport converter, power regulation, soft normally open point.**

Received 27 August 2024; revised 7 November 2024; accepted 14 December 2024. Date of publication 18 December 2024; date of current version 28 January 2025. This work was supported in part by the National Natural Science Foundation of China under Grant 52277193 and in part by the Shanghai Committee of Science and Technology under Grant 23DZ1201202. Recommended for publication by Associate Editor M. Narimani. *(Corresponding authors: Jianwen Zhang; Jianqiao Zhou.)*

The authors are with the Key Laboratory of Control of Power Transmission and Conversion, Shanghai Jiao Tong University, Shanghai 200240, China (e-mail: cjx99290301@sjtu.edu.cn; icebergzjw@sjtu.edu.cn; jianqiaozhou@sjtu.edu.cn; gangshi@sjtu.edu.cn; jiayajun@sjtu.edu.cn; wanghansjtu@sjtu.edu.cn; xucai@sjtu.edu.cn).

Color versions of one or more figures in this article are available at https://doi.org/10.1109/TPEL.2024.3519892.

Digital Object Identifier 10.1109/TPEL.2024.3519892

I. Introduction

With the widespread integration of distributed energy sources and dc loads with strong power fluctuations, traditional distribution networks (DN) confront problems such as voltage violations, bidirectional power flow, and complicated protection design, which threaten the power quality and supply reliability of distribution networks [1]. As an effective solution with application prospect, soft normally open points (SNOPs) based on power electronic devices is initially proposed in [2], as depicted in Fig. 1. By substituting traditional tie switches, the SNOP achieves precise control over both active power and reactive power, and the voltage adjustment of feeders, thereby enhancing the operational viability and controllability of the DN [3], [4]. Typically, the SNOP consists of one or more voltage source converters, which connect the ac and dc grids and share a common dc bus. The medium voltage dc (MVdc) grid established by SNOP has advantages of high supply reliability, high power quality, and easy consumption of new dc sources and loads [5].

Due to the advantages of modularity, scalability, and without limitations of voltage withstand and series voltage equalization technology of switching devices, modular multilevel converter (MMC) has been widely used in multiterminal flexible interconnection projects [6], [7]. The generally adopted BTB-MMC scheme consists of multiple MMC converters. The BTB-MMC scheme require a large number of IGBTs and bulky capacitors, which leads to high costs and a large area occupied for the converter station, hindering further popularization, and application [8].

Currently, in order to achieve compact and low-cost of ac–dc converter stations, several methods have been proposed in related research to improve control strategies [9], [10], [11] or topology structures [12], [13], [14], [15], [16]. On the improvement of control strategies, Kolluri et al. [9] reduced the submodule (SM) capacitor voltage fluctuations by injecting double-frequency circulating current; Samajdar and Bhattacharya [10] proposed an optimization strategy for circulating current injection without using lookup tables to optimize the SM capacitor voltage; Younis et al. [11] presented a double-frequency circulating current suppression strategy based on midpoint capacitor

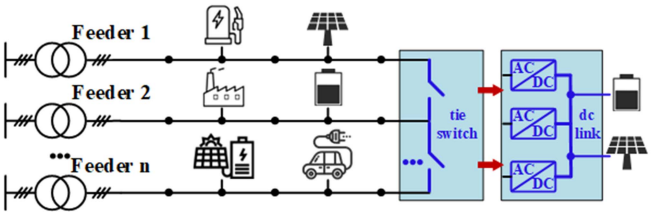

Fig. 1. Structure of DN with the multiport SNOP.

voltage, which can also significantly reduce the number of sensors. In terms of improving topology structures, Li et al. [12] proposed a modified MMC (M-MMC) topology with an intermediate SM, and the top and bottom SMs are interconnected through auxiliary cables. M-MMC can reduce the number of SMs and suppress the double-frequency component of SM capacitor voltage at the same output voltage level compared to the conventional MMC. Huang et al. [13] and Jia et al. [14] both proposed an improved MMC topology by adding a middle SM and corresponding control strategy to reduce the SM capacitance. Le and Lee [15] proposed a novel middle SM that uses less components. Jia et al. [16] proposed an active power decoupling MMC (APD-MMC) topology integrates the APD circuit with the full-bridge SM to reduce the capacitance.

The aforementioned methods are all based on a single MMC and do not alter the fundamental structure of BTB-MMC. The SNOP with BTB-MMC scheme still includes several full-power converters, requiring a large number of switching devices and bulky capacitors, leading to high costs and large volumes.

To address the economic issue of the BTB-MMC scheme, a modular multilevel converter topology with multiple MVac ports (MACP-MMC) is introduced in [17], as shown in Fig. 2(a). A multiport SNOP with MACP-MMC scheme requires only one full-power MMC, which interconnects multiple ac feeders through small-capacity half-bridge converters in the multiport interconnection module (MIM), enabling flexible power flow control. Accordingly, by adding small-capacity half-bridge converters in the MIM, the ac ports expansion can be easily and economically achieved. Therefore, the MACP-MMC scheme offers advantages such as compactness, cost-effectiveness, and ease of scalability. The MACP-MMC is an economical solution but it has some limitations: under certain conditions, when the ac output current of MMC is significantly low, the balance ability of the power balanced control submodule (PBCM) becomes insufficient, leading to fail operation of MACP-MMC.

According to power interaction mode between the MVac feeders and MVdc, the application scenarios of SNOP is divided into the joint supply or consumption scenario and the flexible interconnection scenario. For the joint supply or consumption scenario, the residual capacity of the ac feeders is used to joint supply or consume the power of MVdc, where the distributed energy sources and dc loads are integrated. In addition, the flexible interconnection scenario is also vital and meaningful for the SNOP's application: through mutual power exchange among multiple ac feeders, the load balancing, voltage regulation, and power quality improvement can be achieved [18]. The power flow direction of two scenarios is depicted in Fig. 3.

Without considering the reactive current, whether there is MMC's ac output current is other distinguishable feature between two scenarios. Therefore, due to the MACP-MMC's internal energy balance ability need to be guaranteed by relatively large interaction current of PBCM, it can only apply to the joint supply or consumption scenario but is not suitable for the flexible interconnection scenario. To expand the MACP-MMC's application scenario, this article proposes an enhanced modular multilevel converter with multiple MVac ports (eMACP-MMC), which achieves full-range operation, as depicted in Fig. 2(b). The key to improve the adjustment range of eMACP-MMC is to improve the energy balance ability of PBCMs, which is determined by the amplitude of their interaction current. Therefore, the eMACP-MMC expands a new energy exchange path with the fundamental-frequency circulating current. By adjusting the injected circulating current, the PBCMs' balance ability is always sufficient. The improvements of eMACP-MMC are summarized as follow.

In terms of circuit structure and operating principle, eMACP-MMC improves the connection structure between MMC part and MIM part: the PBCMs are added to two, which connect to the upper and lower arms of the MMC, respectively, providing increased control flexibility and more energy exchange paths. The two PBCMs can interact with both the differential-mode output current and the common-mode circulating current of MMC to achieve the internal energy balance of the MIM part. On the one hand, under the joint supply or consumption scenario, the eMACP-MMC can work as "MACP-MMC mode" where the PBCMs output same voltage. On the other hand, under the flexible interconnection scenario, the energy balance of MIM can be achieved by adjusting the injected the fundamental-frequency circulating current. Consequently, eMACP-MMC can not only apply to the joint supply or consumption scenario as MACP-MMC, but also expand to the flexible interconnection scenario, thus holding a potential application prospect.

Accordingly, an internal energy balance control strategy based on actively injecting circulating current is designed for eMACP-MMC, which is completely different from the MACP-MMC's. The MIM's dc-link voltage is maintained by adjusting the injected fundamental-frequency circulating current through MMC after the PBCMs' output voltages are given based on the optimization method introduced later. However, the aforementioned circulating current may lead to energy imbalance between the arms of the MMC. Therefore, the circulating current's other control degree of freedom is used to balance the upper and lower arms of MMC. Consequently, the circulating current injection control strategy is proposed to achieve function and control decoupling of the circulating current's two components.

Finally, considering that the circulating current has some shortcomings, such as increased current stress, more power loss, and arm currents distortion [19], the eMACP-MMC's redundant degrees of freedom can be used to reduce the actively injected circulating current as possible. Based on the energy balance mechanism of MIM part, the optimization method is proposed

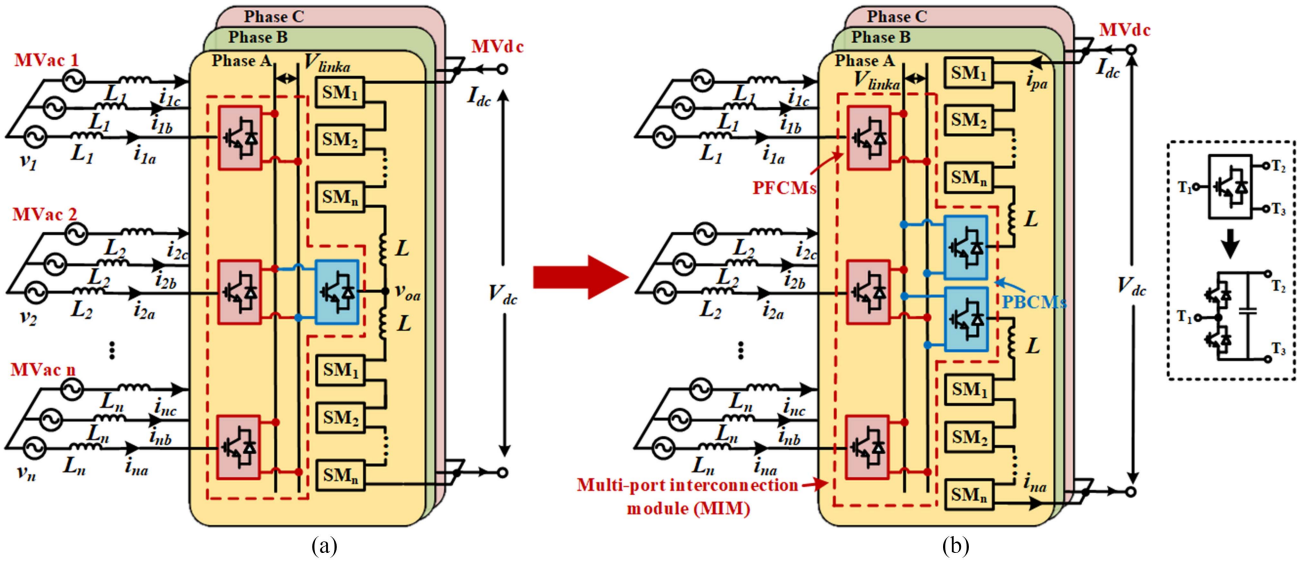

Fig. 2. Converter station topological configurations. (a) Converter station with MACP-MMC scheme. (b) Converter station with eMACP-MMC scheme.

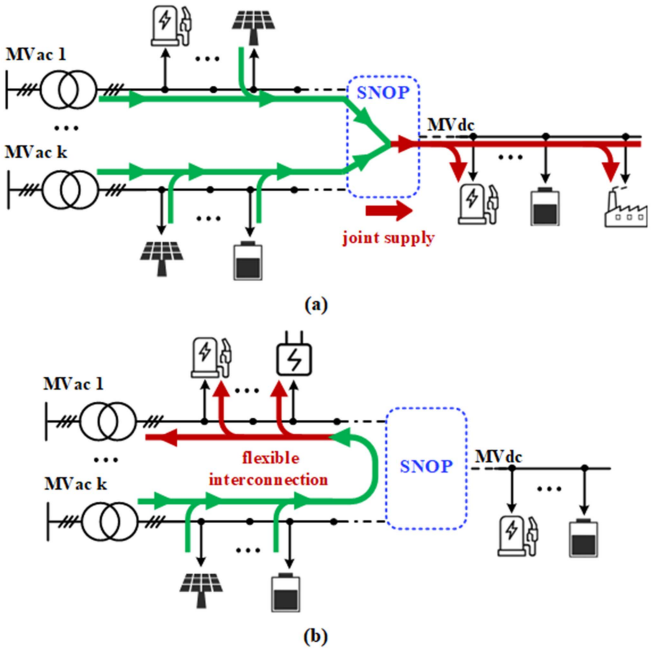

Fig. 3. Power flow direction of two scenarios. (a) Joint supply scenario. (b) Flexible interconnection scenario.

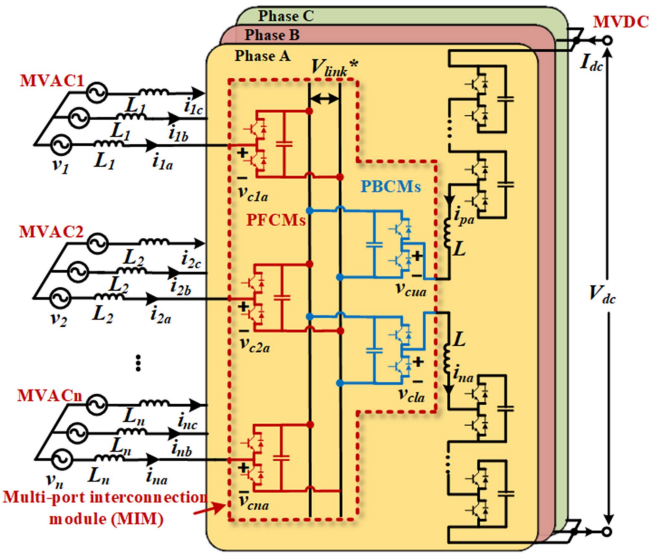

Fig. 4. Hybrid distribution system based on eMACP-MMC scheme.

from two aspects: 1) reducing the power exchange through power flow control submodules (PFCMs) and 2) increasing the power balance efficiency of PBCMs.

The rest of this article is organized as follows. Section II presents the topology structure and power regulation principle. Based on the energy balance mechanism and optimization method introduced in Section III, the corresponding control strategies are designed in Section IV. Section V give a comparison between eMACP-MMC and the existing schemes to further verify its advantages. Section VI demonstrates simulation and experimental results to validate the effectiveness of the proposed topology and control strategies. Finally, Section VII concludes this article.

II. Topology and Power Regulation Principle

A. Topology Configuration

A SNOP with n ac feeders, as illustrated in Fig. 4, which is based on the eMACP-MMC, has two parts: 1) MIM and 2) MMC. The MIM consists of multiple half-bridge SMs (HB-SMs) sharing a low-voltage dc link, which can be further divided into PFCMs and PBCMs based on their respective functions. The ac ports of PFCMs connect to the ac feeders, while the two PBCMs are, respectively, connected to the upper and lower

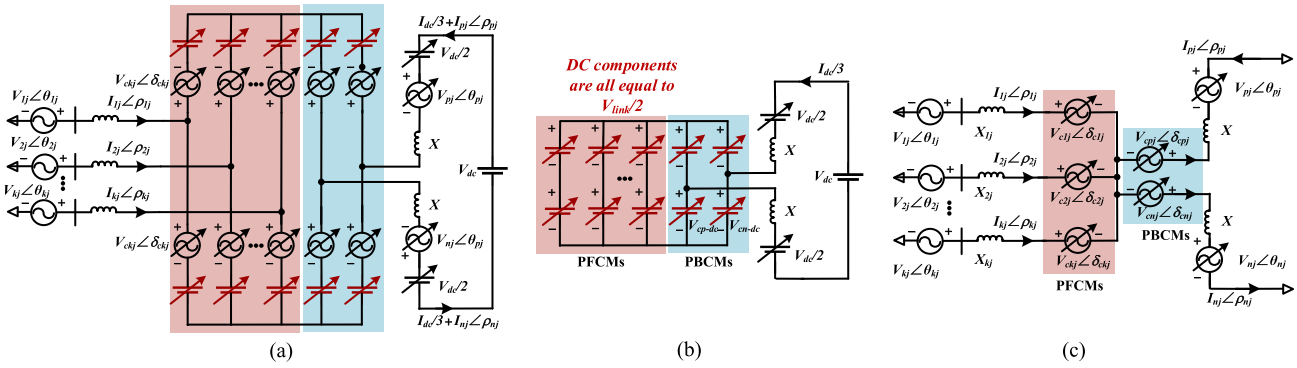

Fig. 5. eMACP-MMC's single-phase equivalent circuits. (a) Overall equivalent circuit. (b) DC equivalent circuit. (c) AC equivalent circuit.

arms of the MMC. The eMACP-MMC exhibits the following characteristics.

1) PFCMs form a series structure between the feeders. Based on the power regulation principle of the series flexible interconnection device [20], the decoupled control of active and reactive power of feeders can be realized by adjusting the series voltages provided by PFCMs between the feeders.
2) PBCMs is used to maintain the internal energy balance of MIM. By improving the connection structure between MMC part and MIM part, a new energy exchange path with PBCMs through circulating current is established in eMACP-MMC. The energy balance of MIM is achieved by injecting fundamental-frequency circulating current through MMC after the PBCMs' voltages is determined by the optimization method, so as to realize the full-range adjustment.
3) eMACP-MMC has economical and flexible ac feeder expansion capability: only need to add small-capacity half-bridge PFCMs on MIM to achieve ac ports expansion.

For the proposed eMACP-MMC topology, the reference directions of variables are illustrated in Fig. 4. The symbols are clarified as follows: k($1 \leq k \leq n$) is the corresponding feeder number, representing Feeder 1 to n; j (j = a, b, c) denotes the phase of the variable, corresponding to phases A, B, and C; v_{kj} and i_{kj}, respectively, indicate the phase-j node voltage and current of kth Feeder. v_{ckj} represents the output voltage at phase j of PFCM, while v_{cpj} and v_{cnj} represent the phase-j output voltages of PBCMS. $V_{\mathrm{link}j}$ denotes the phase-j dc-link voltage, and i_{pa} and i_{na} represent the phase-j currents of MMC's upper and lower arms. L_k denotes the filter inductance on Feeder k, L represents the bridge arm inductance of the MMC, and V_{dc} and I_{dc}, respectively, indicate the voltage and current on the MVdc.

B. Power Regulation Principle

Ignoring the switching-frequency harmonics, the HBSM adopting fully controllable devices can be regarded as a controlled voltage source, which includes dc and ac components, as well as the MMC's arms. The single-phase equivalent circuit of eMACP-MMC is shown in Fig. 5(a). Based on the superposition theorem, the ac equivalent circuit and dc equivalent circuit is shown in Fig. 5(b) and (c), respectively. As for the dc circuit, since SPWM is adopted, to make the most of the modulation range, the dc components of the HBSMs' output voltage are equal to the half of the MIM's dc-link voltage. The dc components do not affect the currents of the feeders, and the power of feeders is only related to the ac equivalent circuit.

In the equivalent circuit, $V_{kj}\angle\theta_{kj}$ and $I_{kj}\angle\rho_{kj}$ represent the phase-j node voltage and line current of Feeder k, $V_{Xkj}\angle\theta_{Xkj}$ represents the phase-j voltage on the equivalent impedance X_{kj} of Feeder k, and $V_{ckj}\angle\delta_{ckj}$ represents the fundamental component of the phase-j output voltage of PFCM connected to Feeder k. Additionally, $V_{cpj}\angle\delta_{cpj}$, $V_{cnj}\angle\delta_{cnj}$ represent the fundamental components of the output voltages of the PBCMs. The inductance of the MMC bridge arm is X, while $V_{pj}\angle\theta_{pj}$, $V_{nj}\angle\theta_{nj}$ and $I_{pj}\angle\rho_{pj}$, $I_{nj}\angle\rho_{nj}$, respectively, denote the phase-j voltage and current of the upper and lower arms of the MMC. For simplification, the following analysis is carried out in single-phase and ignores the subscript j.

In the multiterminal SNOP system, Feeder 1 is selected as the balanced feeder, and its active power is self-balanced according to the active power of the remaining feeders and the MVdc. Therefore, the power of the ports should satisfy the following relationship:

$$P_1 = P_{\mathrm{dc}} - \sum_{k=2}^{n} P_k - P_{\mathrm{loss}} \tag{1}$$

where P_k is the active power of the kth feeder, P_{dc} is the power of MVdc side, and P_{loss} is the system operating loss. In the ac equivalent circuit, the vector relationship between Feeder 1 and Feeder k is shown in Fig. 6. Consequently, the power of the feeder k can be calculated as

$$\begin{aligned} P_k + jQ_k &= (P_{k0} + \Delta P) + j(Q_{k0} + \Delta Q) = \overrightarrow{V}_k \cdot \overrightarrow{I}_k^{conj} \\ &= \overrightarrow{V_k} \cdot \left[\left(\overrightarrow{V}_k - \overrightarrow{V}_1 + \overrightarrow{V}_{X1} + \overrightarrow{V}_{c1} - \overrightarrow{V}_{ck} \right) / jX_k \right]^{conj} \\ &= \overrightarrow{V_k} \cdot \left[\left(\overrightarrow{V}_k - \overrightarrow{V}_1 + \overrightarrow{V}_{X1} + \Delta\overrightarrow{V}_{c1k} \right) / jX_k \right]^{conj}. \end{aligned} \tag{2}$$

The superscript *conj* represents the conjugate of the vector, and $\Delta\overrightarrow{V_{c1k}} (= \overrightarrow{V_{c1}} - \overrightarrow{V_{ck}})$ represents the series regulation voltage between Feeder 1 and Feeder k, which is the difference value of the output voltages of the corresponding PFCMs. P_{k0}

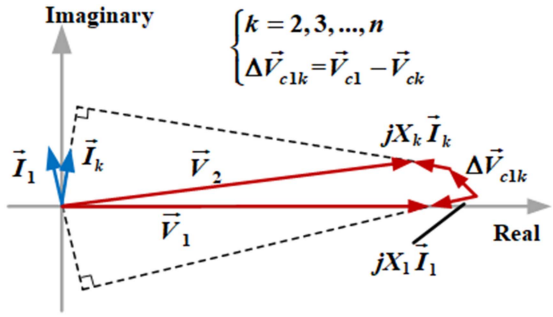

Fig. 6. Phasor diagram of a single-phase ac circuit between feeder 1 and feeder k (=23, …,n).

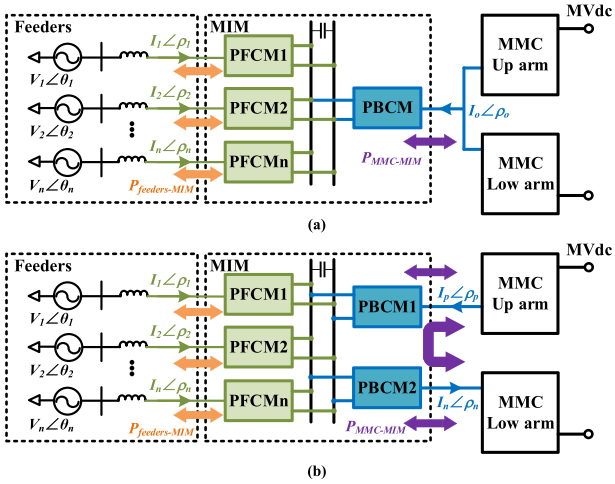

Fig. 7. Energy exchange relationship of MIM. (a) Relationship of MACP-MMC. (b) Relationship of eMACP-MMC.

and Q_{k0} are the natural power flow of feeder k, which is only related to the node voltages of Feeder 1 and Feeder k and the line parameters. ΔP_k and ΔQ_k are the controllable power flow components regulated by the series regulation voltage $\Delta\overrightarrow{V_{c1k}}$. P_{k0}, Q_{k0} and ΔP_k, ΔQ_k are expressed as

$$\begin{cases} P_{k0} = \frac{V_k V_1 \sin(\theta_k-\theta_1)-V_k V_{X1}\sin(\theta_k-\theta_{X1})}{X_k} \\ Q_{k0} = \frac{V_k^2-V_k V_1\cos(\theta_k-\theta_1)+V_k V_{X1}\cos(\theta_k-\theta_{X1})}{X_k} \end{cases} \tag{3}$$

$$\begin{cases} \Delta P_k = -\frac{V_k \Delta V_{c1k}\sin(\theta_k-\delta_{c1k})}{X_k} \\ \Delta Q_k = \frac{V_k \Delta V_{c1k}\cos(\theta_k-\delta_{c1k})}{X_k}. \end{cases} \tag{4}$$

According to (3) and (4), by adjusting the series regulation voltage $\Delta\overrightarrow{V_{c1k}}$, the active power and reactive power of 2-*n*th feeders can be controlled continuously and independently, and the adjustment range is a circle with the radius of $V_k\Delta V_{c1k}/X_k$.

III. Energy Balance Mechanism of eMACP-MMC

In eMACP-MMC, the MIM's dc link consists of several parallel capacitors as energy buffer. While regulating the power of the feeders through PFCMs, there are energy exchange between MIM's dc link and the ac feeders. To achieve normal operation of eMACP-MMC, its PBCMs conduct as an energy balance channel to maintain the MIM's dc-link voltage. However, while the internal energy balance is achieved by adjusting the fundamental-frequency circulating current, it leads to imbalance between the MMC's arms. Therefore, the circulating current's other control degree of freedom is used to balance the upper and lower arms of MMC. Additionally, the eMACP-MMC's redundant control degrees of freedom can be used to optimize the operation by reducing the injected circulation current from two aspects. Since the energy balance mechanism is same in each phase, the following analysis is elaborated in the single-phase case.

A. Energy Balance Mechanism of MIM's Dc Link

According to the energy exchange relationship shown in Fig. 7(a), the energy exchange path between MIM and MMC is unique in MACP-MMC: by adjusting the output voltage of PBCM, it interacts with the MMC's ac output current to maintain the MIM's dc-link voltage. When the phase of PBCM's output voltage is consistent with that of MMC's output current, the energy balance equation of MACP-MMC can be expressed as

$$V_{bl} = \frac{1}{I_o}\left[\sum_{k=1}^{m} V_{ck} I_k \cos(\delta_{ck}-\rho_k)\right], \delta_{bl} = \rho_o. \tag{5}$$

In (5), V_{bl} and δ_{bl} represent the amplitude and phase of the output voltage of PBSM, respectively, while I_o and ρ_o is the amplitude and phase of MMC's ac output current. From (5), when I_o is extremely small, the balance ability of PBCM is insufficient, leading to fail operation of MACP-MMC.

The proposed eMACP-MMC expands a new energy exchange path, and improves the balance ability of PBCMs by actively injecting fundamental-frequency circulating current. If only the dc and fundamental-frequency components are considered, the average switching functions of PFCMs and PBCMs are shown in (6), and the feeders' current and the MMC's output current can be expressed as (7)

$$\begin{cases} v_{ck}(t) = \sqrt{2}V_{ck}\sin(\omega t+\delta_{ck}) + V_{\text{link}}/2, k=1,\ldots,n \\ v_{cp}(t) = \sqrt{2}V_{cp}\sin(\omega t+\delta_{cp}) + V_{\text{link}}/2 \\ v_{cn}(t) = \sqrt{2}V_{cn}\sin(\omega t+\delta_{cn}) + V_{\text{link}}/2 \end{cases} \tag{6}$$

$$\begin{cases} i_k(t) = \sqrt{2}I_k\sin(\omega t+\rho_k) \\ i_o(t) = \sum_{k=1}^{n} i_k(t) = \sqrt{2}I_o\sin(\omega t+\rho_o). \end{cases} \tag{7}$$

Considering the symmetry among the phases of MMC and between the upper and lower arms, the MVdc current is evenly divided into three phases, and the current of MMC's ac port is equally divided into the upper and lower arms. Therefore, the circulating current can be expressed as (8), which includes dc and fundamental-frequency components. Furthermore, the current of upper and lower arms can be expressed as (9)

$$i_{cir}(t) = \sqrt{2}I_{cir}\sin(\omega t+\rho_{cir}) + I_{\text{dc}}/3 \tag{8}$$

$$\begin{cases} i_p(t) = -\frac{\sqrt{2}}{2} I_o \sin(\omega t + \rho_0) + \sqrt{2} I_{cir} \sin(\omega t + \rho_{cir}) + \frac{I_{\text{dc}}}{3} \\ i_n(t) = \frac{\sqrt{2}}{2} I_o \sin(\omega t + \rho_0) + \sqrt{2} I_{cir} \sin(\omega t + \rho_{cir}) + \frac{I_{\text{dc}}}{3}. \end{cases} \tag{9}$$

The current flowing into the MIM's dc-link capacitor is equal to the product of the ac ports' current and the average switching functions of the HBSMs, which can be expressed as

$$i_{\text{link}}(t) = \sum_{k=1}^{n} (s_{ck} \times i_k) + s_{cp} \times i_p - s_{cn} \times i_n. \tag{10}$$

In addition to the dc component, there are fundamental-frequency and double-frequency fluctuations in i_{link}. In order to maintain the energy balance of MIM's dc link, the dc component in i_{link} must be 0, as (11) depicted

$$\begin{aligned} &\sum_{k=1}^{n} V_{ck} I_k \cos(\delta_{ck} - \rho_k) \\ &\quad - 0.5 V_{cp} I_o \cos(\delta_{cp} - \rho_o) - 0.5 V_{cn} I_o \cos(\delta_{cn} - \rho_o) \\ &\quad + V_{cp} I_{cir} \cos(\delta_{cp} - \rho_{cir}) - V_{cn} I_{cir} \cos(\delta_{cn} - \rho_{cir}) = 0. \end{aligned} \tag{11}$$

It can be seen from (11) that the energy exchange channels between MIM and MMC is extended by improving the structure between the MMC part and MIM part, as shown in Fig. 7(b). Considering the fundamental-frequency component, based on the reference direction shown in Fig. 5(c), on the one hand, the common-mode component of the PBCMs' output voltages can interact with the output current of the MMC; on the other hand, the differential-mode component can interact with the MMC's circulating current.

When it applies to the joint supply and consumption scenario, the proposed eMACP-MMC can also operate in "MACP-MMC mode". When the constraint in (12) is satisfied, the eMACP-MMC's equivalent circuit is the same as the MACP-MMC's, so as the internal energy balance mechanism

$$V_{cp} \angle \delta_{cp} = V_{cn} \angle \delta_{cn}. \tag{12}$$

When it comes to the flexible interconnection scenario, the MMC's output current is quite small. Therefore, eMACP-MMC maintains the energy balance of MIM by adjusting the injected fundamental-frequency circulating current after the output voltages of PBCMs are determined by the optimization method. Base on the above internal energy balance mechanism, the SNOP with eMACP-MMC scheme can operate in full range, theoretically.

The circulating current component used for MIM's dc-link energy balance is recorded as $i_{cir\perp}$. However, $i_{cir\perp}$ may lead to energy imbalance between the upper and lower arms of MMC, so it is necessary to apply the circulating current's other control degree of freedom to eliminate the flaw. The other component is denoted as $i_{cir\parallel}$, which is perpendicular to $i_{cir\perp}$. The energy exchange relationship related to the two components of circulating current is depicted in Fig. 8.

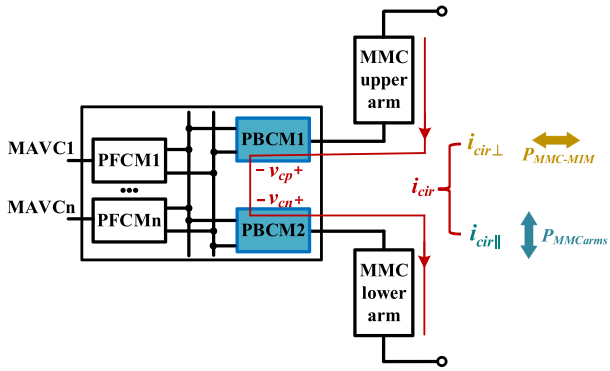

Fig. 8. Energy exchange relationship related to the two components of circulating current.

B. Optimization Method for Minimizing the Circulating Current

The circulating current has some shortcomings, such as increased current stress, more power loss, and arm currents distortion [19]. Furthermore, there are several redundant control degrees of freedom in eMACP-MMC, such as the output voltage of PFCM connecting to the balanced feeder, the PBCMs' output voltages, and the phase of the circulating current. These redundant degrees of freedom can be used to optimize the system by reducing the injected circulating current. When the output current of MMC is close to zero, the energy balance equation of MIM is expressed as

$$\begin{aligned} &2 V_{c\_diff} I_{cir} \cos\left(\delta_{c\_diff} - \rho_{cir}\right) \\ &\quad = -\sum_{k=1}^{n} V_{ck} I_k \cos\left(\delta_{ck} - \rho_k\right) + P_{\text{loss}} \end{aligned} \tag{13}$$

where V_{c_diff} and δ_{c_diff} represent the amplitude and phase of the PBCMs' differential-mode output voltage, I_{cir} and ρ_{cir} represent the amplitude and phase of the circulating current, and P_{loss} represents the internal power loss of MIM part. Recording

$$\Delta P = -\sum_{k=1}^{n} V_{ck} I_k \cos(\delta_{ck} - \rho_k) \tag{14}$$

where ΔP represents the power exchange between MIM and the feeders through PFCMs. Therefore, the optimization method can be considered as two aspects. On the one hand, the redundant degrees of freedom of PFCM are used to reduce the power interaction between MIM and the feeders through PFCMs, namely reduce ΔP. On the other hand, the PBCMs' output voltages and the phase of the circulating current are selected to increase the energy balance ability through the PBCMs and the circulating current.

First, the output voltage of PFCM connecting to the balanced feeder is optimized to reduce the energy exchange between MIM and the feeders. In eMACP-MMC, the PFCMs output several equivalent series voltages to regulated the power of the feeders. Then, the output voltage of each PFCM can be expressed as

$$\overrightarrow{V}^*_{ck} = \overrightarrow{V}^*_{c1} - \Delta \overrightarrow{V}^*_{c1k} (k = 2, 3, \ldots, n) \tag{15}$$

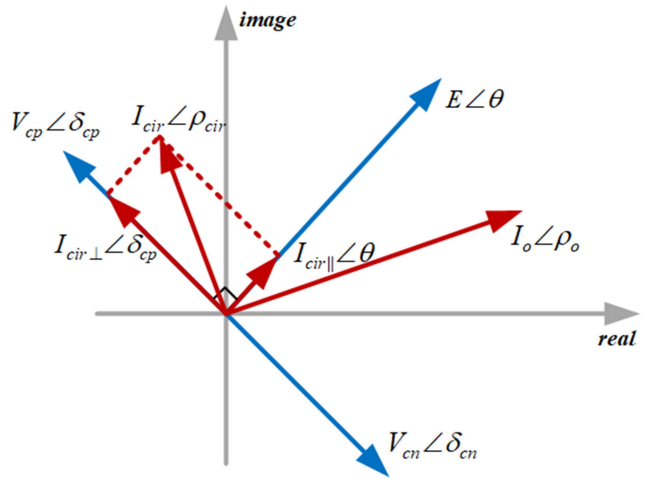

Fig. 9. Phasor diagram of fundamental-frequency circulating current and the related variables.

where $\Delta\overrightarrow{V}^*_{c1k}$ represents the series voltages, $\overrightarrow{V}^*_{c1}$ is the reference output voltage of PFCM connecting to the balanced feeder, and $\overrightarrow{V}^*_{ck}$ represents the reference output voltages of PFCMs connecting to the normal feeders. Therefore, the $\overrightarrow{V}^*_{c1}$ can be determined by the principle of reducing the power interaction between MIM and the feeders (ΔP). The value of $\overrightarrow{V}^*_{c1}$ in different working condition can be obtained by look-up table.

Second, the PBCMs' output voltages and the phase of the circulating current are optimized to increase the energy balance ability through the PBCMs and the circulating current. When the phase of PBCM's output voltages is consistent with the phase of $i_{cir\perp}$, the amplitude of $i_{cir\perp}$ is lowest. Besides, since $i_{cir\parallel}$ is perpendicular to the PBCMs' output voltages, the energy balance of MIM is not affected by $i_{cir\parallel}$, and then the function decoupling of $i_{cir\perp}$ and $i_{cir\parallel}$ can be realized. Additionally, when $i_{cir\perp}$ is perpendicular to MMC's ac output voltage, the energy transfer between MMC's the upper and lower arms can be reduced, thereby significantly reducing $i_{cir\parallel}$. In summary, the PBCMs' output voltages, the MMC's ac output voltage and current, and the two components of the circulating current satisfy the phase relationship in (16), as shown in Fig. 9. Furthermore, the amplitude of PBCMs' output voltage is given in (17), where a certain margin is considered while making most of its modulation range

$$\begin{cases}\delta_{cp}=\theta+\frac{\pi}{2} & \begin{cases}\rho_{cir\perp}=\delta_{cp}\\ \rho_{cir\parallel}=\theta\end{cases}\\ \delta_{cn}=\theta-\frac{\pi}{2}\end{cases} \tag{16}$$

$$V_{cp}=V_{cn}=\frac{0.9*V_{\text{link}}}{2}. \tag{17}$$

Combining (11) and (16), the energy balance equation of MIM can be expressed as

$$\sum_{k=1}^{n}V_{ck}I_k\cos(\delta_{ck}-\rho_k)-(V_{cp}+V_{cn})I_{cir\perp}=0. \tag{18}$$

TABLE I
CIRCULATING CURRENT OF MMC PART

	Case1	Case2	Case3	Case4
Circulating current before optimized (RMS)/A	11.91	28.33	2.77	25.42
Circulating current after optimized (RMS)/A	2.24	2.57	1.51	1.22

From (18), under the flexible interconnection scenario, the energy balance of MIM can be realized by adjusting the fundamental-frequency circulating current of MMC after the PBCMs' output voltages are given. Consequently, the eMACP-MMC achieves full-range operation.

Based on the simulation results, the rms value of the fundamental-frequency circulating current in each working case is shown in Table I. The optimized results show that the proposed optimized method can significantly reduce the injected circulating current.

C. Energy Balance Mechanism Between MMC Arms

The circulating current's other control degree of freedom is used to eliminate the imbalance between the MMC's arms caused by the former component. Aiming at analyzing the energy balance mechanism between the MMC's arms, the SM capacitor currents of them are analyzed. The MMC's equivalent output voltage is expressed as

$$e(t)=\sqrt{2}E\sin(\omega t+\theta). \tag{19}$$

Ignoring the internal losses, the overall energy balance of the eMACP-MMC satisfies (20). Equation (21) is given to simplify the following expressions:

$$\sum_{k=1}^{n}V_{ck}I_k\cos(\delta_{ck}-\rho_k)+EI_o\cos(\theta-\rho_o)+\frac{V_{\text{dc}}I_{\text{dc}}}{3}=0 \tag{20}$$

$$\begin{cases}\Delta P=V_{ck}I_k\cos(\delta_{ck}-\rho_k)\\ K=EI_o\cos(\theta-\rho_o)+\frac{V_{\text{dc}}I_{\text{dc}}}{3}.\end{cases} \tag{21}$$

The differential-mode component of PBCM's output voltages constitute a common-mode component in MMC, which is similar to the circulation. In order to avoid introducing unnecessary circulating current, the PBCMs' output voltages are compensated in the MMC's arms. Additionally, the MMC also needs the voltage component for injecting the fundamental-frequency circulating current. Only considering the dc and fundamental-frequency components, the average switching function of the MMC upper and lower arms can be expressed as

$$\begin{cases}S_p=\frac{0.5V_{\text{dc}}-e-v_{cir1}-v_{cp}}{V_{\text{dc}}}\\ S_n=\frac{0.5V_{\text{dc}}+e-v_{cir1}+v_{cn}}{V_{\text{dc}}}\end{cases} \tag{22}$$

where V_{dc} represents the voltage of MVdc, and e represents the MMC's differential-mode output voltage. The v_{cir1} is the voltage for circulating current injection, and v_{cp} and v_{cn} are the PBCMs' reference output voltages.

Combining (9) and (22), the SM capacitor currents of the MMC's arms can be expressed as

$$\begin{cases} i_{cp} = C\frac{du_{cp}}{dt} = S_p \times i_p \\ i_{cn} = C\frac{du_{cn}}{dt} = S_n \times i_n \end{cases} \tag{23}$$

where u_{cp}, u_{cn} and i_{cp}, i_{cn} are the SM capacitor voltages and currents of the MMC's upper and lower arms, respectively. From (23), the SM capacitor currents of MMC includes dc, fundamental-frequency, and double-frequency components. Similar to the analysis of MIM's energy balance, to achieve the energy balance between the MMC's arms, the dc components in the SM capacitor currents must be 0, as depicted in

$$\begin{cases} \frac{K}{2} - \frac{V_{\text{link}}I_{\text{dc}}}{6} - EI_{cir\|} + \left[\frac{1}{2}\omega LI_oI_{cir\|}\cos\left(\theta+\frac{\pi}{2}-\rho_o\right)\right. \\ \quad \left. -\frac{1}{2}\omega LI_oI_{cir\perp}\cos\left(\theta-\rho_o\right)\right] \\ \quad -V_{cp}I_{cir\perp} + \frac{1}{2}V_{cp}I_o\cos(\delta_{cp}-\rho_o) = 0 \\ \frac{K}{2} + \frac{V_{\text{link}}I_{\text{dc}}}{6} + EI_{cir\|} - \left[\frac{1}{2}\omega LI_oI_{cir\|}\cos\left(\theta+\frac{\pi}{2}-\rho_o\right)\right. \\ \quad \left. -\frac{1}{2}\omega LI_oI_{cir\perp}\cos\left(\theta-\rho_o\right)\right] \\ \quad -V_{cn}I_{cir\perp} + \frac{1}{2}V_{cn}I_o\cos(\delta_{cn}-\rho_o) = 0. \end{cases} \tag{24}$$

Combining (16), (20), (21), and (24), the amplitude of $i_{cir\|}$ can be expressed as

$$I_{cir\|} = \frac{-\frac{V_{\text{link}}I_{\text{dc}}}{3} - \omega LI_oI_{cir\perp}\cos(\theta-\rho_o) - \frac{\Delta PI_o\cos(\delta_{cp}-\rho_o)}{2I_{cir\perp}}}{2E - \omega LI_o\cos(\theta+\frac{\pi}{2}-\rho_o)}. \tag{25}$$

IV. Control Strategies of eMACP-MMC

A. Power Flow Control of Feeder 2-nth

The power flow control of eMACP-MMC adopts a classical dual-loop control strategy. Taking the node voltage of feeder 1 as the reference direction, through Park transformation, the power flow of Feeder k is expressed as (26), where the reference value of current inner loop is calculated

$$\begin{cases} P_k^* = \frac{3}{2}(v_{kd}i_{kd}^* + v_{kq}i_{kq}^*) \\ Q_k^* = \frac{3}{2}(v_{kq}i_{kd}^* - v_{kd}i_{kq}^*) \end{cases} \Rightarrow \begin{cases} i_{kd}^* = \frac{2}{3}\frac{v_{kd}P_k^* + v_{kq}Q_k^*}{v_{kd}^2+v_{kq}^2} \\ i_{kq}^* = \frac{2}{3}\frac{v_{kq}P_k^* - v_{kd}Q_k^*}{v_{kd}^2+v_{kq}^2}. \end{cases} \tag{26}$$

In (26), P_k and Q_k are the Feeder k's (= 2, …, n) reference values of active power and reactive power, respectively, and the subscripts d and q represent the *d*-axis and *q*-axis components.

The current inner loop for rapidly tracking the reference current, is analyzed below. Based on KVL, the dynamic equation between Feeder 1 and Feeder k is established as

$$v_{1j} - R_1i_{1j} - L_1\frac{di_{1j}}{dt} - \Delta v_{c1kj} = v_{kj} - R_ki_{kj} - L_k\frac{di_{kj}}{dt} \tag{27}$$

where R_k and L_k represent the resistance and filter inductance of Feeder k, respectively. Δv_{c1kj} represents the series voltage generated by PFCMs between Feeder 1 and Feeder k. Then, Park transformation is performed on (27) to obtain the expression in the *dq*-axis. Furthermore, the control equation of the inner loop

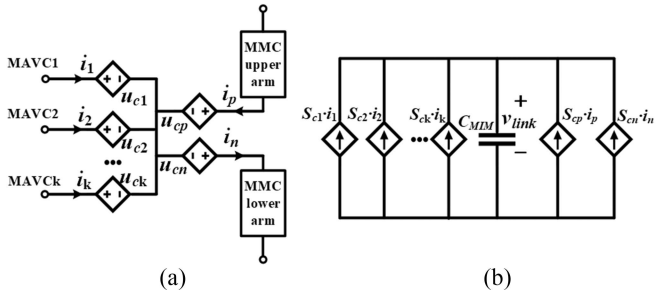

Fig. 10. Single-phase equivalent circuit of MIM part. (a) External output equivalent circuit. (b) Internal capacitor dynamic equivalent circuit.

is obtained as

$$\begin{cases} \Delta v_{c1kd}^* = k_{p1}(i_{kd}^* - i_{kd}) + k_{i1}\int(i_{kd}^* - i_{kd})dt \\ \qquad\qquad +v_{1d} - v_{kd} - \omega L_ki_{kq} + \omega L_1i_{1q} \\ \Delta v_{c1kq}^* = k_{p1}(i_{kq}^* - i_{kq}) + k_{i1}\int(i_{kq}^* - i_{kq})dt \\ \qquad\qquad +v_{1q} - v_{kq} + \omega L_ki_{kd} - \omega L_1i_{1d} \end{cases} \tag{28}$$

where the reference series voltages Δv_{c1kd}^* and Δv_{c1kq}^* in the *dq*-axis can be obtained. Through inverse Park transformation, the reference value Δv_{c1kabc}^* in the *abc*-axis can be calculated.

B. Energy Balance Control by Actively Injecting Fundamental-Frequency Circulating Current Through MMC

According to the control targets, the actively injected fundamental-frequency circulating current is divided into two mutually perpendicular components, so as to realize decoupled control. The fundamental-frequency circulating current injection control adopts a double closed-loop control strategy: the outer loop obtains the reference currents value in the *dq*-axis according to the corresponding control target. The current inner loop makes the actual fundamental-frequency circulating current track its reference value quickly by adjusting the corresponding voltage components of the MMC's arms. Based on the control targets: the energy balance of MIM's dc link and the energy balance between the upper and lower arms of MMC, the PI controller is used to eliminate the error, and the voltage outer loop can be obtained.

For a three-phase balance system, the MIM's dynamic analysis of each phase is similar. Therefore, according to the detailed structure of eMACP-MMC shown in Fig. 4, the single-phase circuit of MIM part is obtained in Fig. 10, where the external output equivalent circuit and the internal capacitor dynamic equivalent circuit is depicted in Fig. 10(a) and (b), respectively. In Fig. 10, i_m ($m = 12,\ldots$,k) are the currents of the feeders; u_{cm} ($m = 12,\ldots$,k) are the output voltage of PFCMs; i_p and i_n are the currents of MMC's upper and lower arms; u_{cp} and u_{cn} are the output voltages of PBCMs; S_{cm} ($m = 12,\ldots$,k) are the average switching functions of PFCMs; S_{cp} and S_{cn} are the average switching functions of PBCMs; v_{link} is the capacitor voltage of MIM; C_{MIM} is the capacitance of MIM's dc link.

The instantaneous power of MIM is expressed as

$$\sum_{m=1}^{k} u_{cm} \times i_m + u_{cp} \times i_{cp} + u_{cn} \times i_{cn} = C_{\text{MIM}} V_{\text{link}} \frac{d\Delta v_{\text{link}}}{dt}. \tag{29}$$

The average switching functions of PFCMs and PBCMs is expressed as

$$\begin{cases} S_{cm} = \frac{u_{cm}}{V_{\text{link}}^*} + \frac{1}{2}, m = 1, 2, \ldots, k \\ S_{cp} = \frac{u_{cp}}{V_{\text{link}}^*} + \frac{1}{2} \\ S_{cn} = \frac{u_{cn}}{V_{\text{link}}^*} + \frac{1}{2} \end{cases} \tag{30}$$

where $V_{\text{link}*}$ is the reference value of MIM's dc-link voltage. To maximum the power interaction efficiency with the circulating current, the PBCMs' output voltages satisfy

$$u_{cp} = -u_{cn}. \tag{31}$$

The currents flowing into the MIM satisfy

$$\begin{cases} \sum_{m=1}^{k} i_m = i_o = i_p - i_n \\ i_{cir} = \frac{1}{2}(i_p + i_n) \end{cases} \tag{32}$$

where i_o represents the MMC's equivalent output current; icir is the circulating current of MMC. Combining (29)–(32), the MIM's capacitor voltage difference equation could be expressed as

$$C_{\text{MIM}} V_{\text{link}} \frac{d\Delta v_{\text{link}}}{dt} = \sum_{m=1}^{k} u_{cm} \times i_m + 2u_{cp} \times i_{cir}. \tag{33}$$

Equation (33) shows that there is power interaction with PFCMs and the currents of the feeders. By adjusting the circulating current, it interacts with PBCMs to counteract the former power interaction so that maintain the energy balance of MIM part.

Superimposing (33) of three phases, and aligning the reference direction of Park transformation to the MMC's differential-mode output voltage, the MIM's total capacitor voltage difference equation could be rewritten as

$$C_{\text{MIM}} V_{\text{link}} \frac{d\sum_{j=a,b,c} \Delta v_{\text{link}j}}{dt} = P_{\text{MIM\_feeders}} + 3U_{cpq} \cdot I_{cirq} \tag{34}$$

where $u_{cpd} = 0$ since u_{cp} is perpendicular to the reference direction of Park transformation. Finally, the MIM's total energy balance control equation can be obtained as

$$I_{cirq}{}^* = \left(k_{p1} + \frac{k_{i1}}{s}\right)\left(\sum_{j=a,b,c} v_{\text{link}j} - 3V_{\text{link}}{}^*\right) - \frac{P_{\text{MIM\_feeders}}}{3U_{cpq}}. \tag{35}$$

For a three-phase balance system, the MMC's dynamic analysis of each phase is similar. Therefore, the single-phase circuit of MMC part in Fig. 11 is used for analysis. In Fig. 11, u_p and u_n are the MMC's upper and lower arm voltages; i_p and i_n are the MMC's upper and lower arm currents; u_{cp} and u_{cn} are the output voltages of PBCMs; i_o is the output current of MMC; S_p and S_n are the average switching functions of MMC's upper and lower arms; v_{cp} and v_{cn} are SM capacitor voltages of MMC's upper and lower arms; $C_\Sigma = C/N$ is the equivalent arm capacitance.

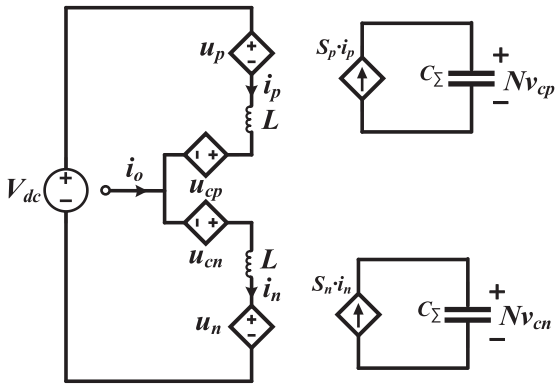

Fig. 11. Single-phase equivalent circuit of MMC part.

The instantaneous arm power equations are derived as

$$\begin{cases} u_p \times i_p = NCv_{cp} \times \frac{dv_{cp}}{dt} \\ u_n \times i_n = NCv_{cn} \times \frac{dv_{cn}}{dt}. \end{cases} \tag{36}$$

The arm voltage in (36) could be expressed as

$$\begin{cases} u_p = N \times S_p \times v_{cp} \\ u_n = N \times S_n \times v_{cn}. \end{cases} \tag{37}$$

For S_p and S_n, the dc and differential-mode ac components are concluded. In addition, to inject fundamental-frequency circulating current and counteract the PBCMs' output voltages, circulating voltage u_{cir} and compensation voltage u_{cp}, u_{cn} (= -u_{cp}) should be added

$$\begin{cases} S_p = \frac{1}{2} + \frac{-e - u_{cir} - u_{cp}}{V_{\text{dc}}} \\ S_n = \frac{1}{2} + \frac{e - u_{cir} - u_{cp}}{V_{\text{dc}}}. \end{cases} \tag{38}$$

The dynamic equation of the circulating current is derived as follows:

$$2L\frac{di_{cir}}{dt} = V_{\text{dc}} - (u_p + u_n + 2u_{cp}). \tag{39}$$

Recording that $u_{\Sigma c} = Nv_{cp} + Nv_{cn}$ and $u_{\Delta c} = Nv_{cp} - Nv_{cn}$ are the sum of the capacitor voltages and the difference of capacitor voltages in two arms. Assuming $u_{\Sigma c} \approx 2V_{\text{dc}}$ and combining (37), (38), and (39), the circulating current dynamic equation could be expressed as

$$L\frac{di_{cir}}{dt} = u_{cir} + \frac{u_{\Delta c} \cdot e}{2V_{\text{dc}}}. \tag{40}$$

Equation (40) indicates that the injection of the circulating current could be achieved via u_{cir}.

Superimposing (40) of three phases, and aligning the reference direction of Park transformation to the MMC's differential-mode output voltage, the circulating current dynamic equation could be rewritten as

$$L\frac{d}{dt}\begin{pmatrix} I_{cird} \\ I_{cirq} \end{pmatrix} = \begin{pmatrix} & \omega L \\ -\omega L & \end{pmatrix}\begin{pmatrix} I_{cird} \\ I_{cirq} \end{pmatrix} + \begin{pmatrix} U_{cird} \\ U_{cird} \end{pmatrix}. \tag{41}$$

Therefore, the inner-loop circulating current control equation can be obtained as

$$\begin{pmatrix} {U_{cird}}^* \\ {U_{cirq}}^* \end{pmatrix} = \left(k_{p3} + \frac{k_{i3}}{s}\right) \begin{pmatrix} {I_{cird}}^* - I_{cird} \\ {I_{cird}}^* - I_{cirq} \end{pmatrix} - \begin{pmatrix} & \omega L \\ -\omega L & \end{pmatrix} \begin{pmatrix} I_{cird} \\ I_{cirq} \end{pmatrix}. \tag{42}$$

Moreover, combining (36), (37), and (38), the capacitor energy dynamic equation could be expressed as

$$C_\Sigma u_{\Sigma c} \cdot \frac{du_{\Sigma c}}{dt} = \frac{V_{\rm dc} I_{\rm dc}}{3} + \frac{V_{\rm dc} i_{cir}}{2} + e i_o - \frac{2u_{cp} I_{\rm dc}}{3} - 2u_{cp} i_{cir} \tag{43}$$

$$C_\Sigma u_{\Sigma c} \cdot \frac{du_{\Delta c}}{dt} = -\frac{V_{\rm dc} i_o}{2} - \frac{2eI_{\rm dc}}{3} - 2ei_{cir} + u_{cp} i_o. \tag{44}$$

Equation (43) is the total capacitor energy equation, the power term $\frac{V_{\rm dc} i_{cir}}{2}$ is the ac component, and power term $-2u_{cp}i_{cir}$ is the power transmitted from MMC to MIM to maintain the energy balance of MIM. Therefore, the injection of fundamental-frequency circulating current will not affect the total capacitor energy of eMACP-MMC.

According to the different control targets, the fundamental-frequency circulating current i_{cir} is decomposed into two mutually perpendicular components, namely $i_{cir\perp}$ and $i_{cir\parallel}$. Among them, the $i_{cir\perp}$ is used for overall energy balance of MIM part, and the $i_{cir\parallel}$ is responsible for internal energy balance between MMC's arms. Since $i_{cir\perp}$ is perpendicular to e, the power term $ei_{cir\perp}$ is equal to 0. Equation (44) is rewritten as

$$C_\Sigma u_{\Sigma c} \cdot \frac{du_{\Delta c}}{dt} = -\frac{V_{\rm dc} i_o}{2} - \frac{2eI_{\rm dc}}{3} + u_{cp} i_o - 2ei_{cir\parallel}. \tag{45}$$

Equation (45) is the arm capacitor energy difference equation. The power term $u_{cp}i_o$ will result in arm energy difference, i.e., the dc component of $u_{\Delta c}$ is not 0 and the capacitor voltages of upper and lower arms are deviated. Therefore, the power term $-2ei_{cir\parallel}$ which contains the other component (control degree of freedom) of circulating current is used to counteract the energy difference.

Superimposing (45) of three phases, and aligning the reference direction of Park transformation to the MMC's differential-mode output voltage, the arm capacitor energy difference equation is rewritten as

$$C_\Sigma u_{\Sigma c} \cdot \frac{d\sum_{j=a,b,c} u_{\Delta cj}}{dt} = \frac{3}{2} U_{cpq} I_{oq} - 3E_d I_{cird}. \tag{46}$$

Finally, the MMC's upper and lower arms energy balance control equation can be obtained as

$${I_{cird}}^* = \left(k_{p2} + \frac{k_{i2}}{s}\right) \left(\sum_{j=a,b,c} (Nv_{cp} - Nv_{cn}) \right) + \frac{U_{cpq} I_{oq}}{E_d}. \tag{47}$$

Consequently, based on the differential (33), (40), (43), and (45), the MIM's and MMC's internal dynamics is revealed, and the corresponding control (35), (42), and (47) are obtained. The proportional and integral coefficients of PI controller can be calculated based on the stability criterion described in [21].

C. Indirect Power Flow Control of Feeder 1 by MMC

Feeder 1 is set as the balanced feeder, whose active power is self-balanced according to the energy balance constraint of the whole system, as expressed in (1). The other feeders can realize decoupling control of active and reactive power, as shown in Fig. 12(a). On this basis, the indirect regulation of the active and reactive power of Feeder 1 can be realized through MMC's control.

The outer loop control of active power is similar to the conventional MMC's: dc voltage control or dc-side active power control can be adopted. Then, the active power of other ports except feeder 1 is under control, and the active power of Feeder 1 is self-balanced with constraint of system energy balance. Similarly, since that the reactive power of Feeder 2-n is determined, the sum of the q-axis reference currents of all ac feeders is used as the q-axis reference value of MMC's inner loop to realize the indirect control of the reactive power of Feeder 1. Therefore, when given the reactive power reference value Q_1^* of Feeder 1, according to KCL and (26), the MMC's q-axis reference current i_{oq}^* can be calculated, as shown in

$$\begin{cases} i_{oq}^* = i_{1q}^* + \sum_{k=2}^{n} i_{kq}^* \\ Q_1^* = \frac{3}{2}\left(v_{1q} i_{1d}^* - v_{1d} i_{1q}^*\right) = -\frac{3}{2} v_{1d} i_{1q}^*. \end{cases} \tag{48}$$

D. Clustered Balancing Control of MIM

The internal energy balance among MIM's three-phase is necessary. Based on the method proposed in [22], a zero-sequence voltage component is superimposed on the PBCM of MACP-MMC to maintain the balance among three phases. However, when the MMC's output current is quite small under some specific conditions, the method also fails.

To eliminate the limitation of MACP-MMC, a zero-sequence voltage component is superimposed on one of the eMACP-MMC's PFCMs to interact with the feeder current, which can avoid the insufficient adjustment ability caused by little current. In order to reduce the amplitude of the injected zero-sequence voltage, the zero-sequence voltages are injected into the PFCM with the largest feeder current. The injected zero-sequence voltage is expressed as

$$v_{bl}^0 = \Delta u_a \sin(\omega t + \rho_o)\, \Delta u_b \sin\left(\omega t + \rho_o - \frac{2}{3}\pi\right) + (-\Delta u_a - \Delta u_b) \sin\left(\omega t + \rho_o + \frac{2}{3}\pi\right) \tag{49}$$

where Δu_a and Δu_b are the output of the P controller, as given in

$$\begin{cases} \Delta u_a = -k_{p3}\left[\left(\sum_{j=a,b,c} V_{{\rm link}j}\right)/3 - V_{{\rm link}a}\right] \\ \qquad = -k_{p3} \Delta V_{{\rm link}a} \\ \Delta u_b = -k_{p3}\left[\left(\sum_{j=a,b,c} V_{{\rm link}j}\right)/3 - V_{{\rm link}b}\right] \\ \qquad = -k_{p3} \Delta V_{{\rm link}b} \end{cases} \tag{50}$$

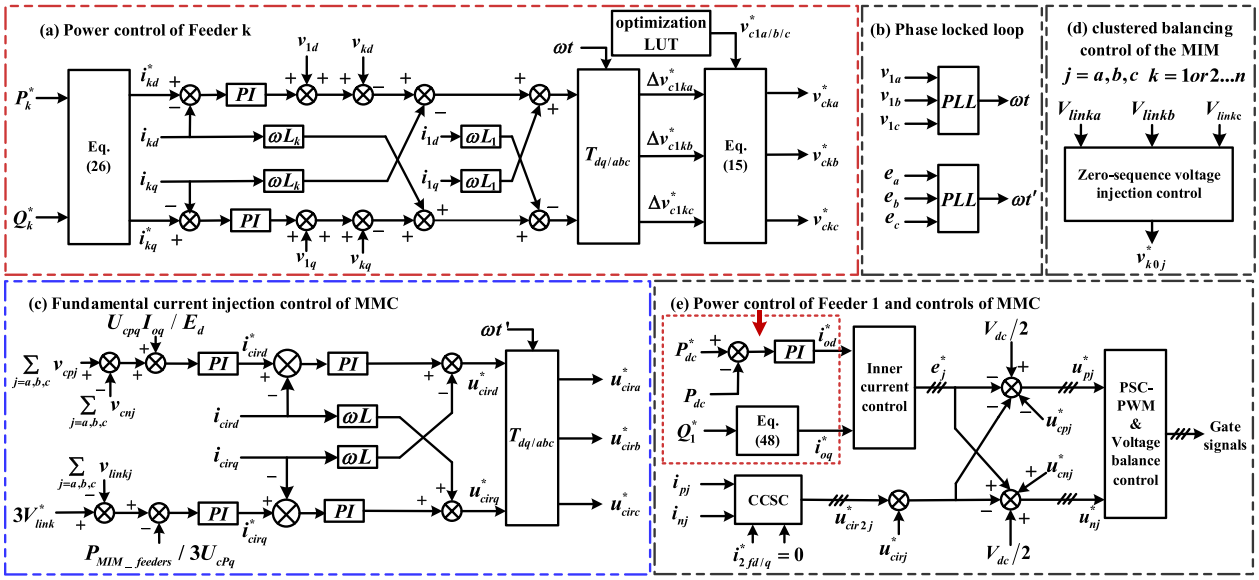

Fig. 12. Control strategies of eMACP-MMC.

where k_{p3} represents the proportional coefficient of the P controller. The injected zero-sequence voltage interacts with the corresponding feeder current $i_{ka/b/c}$ to transfer energy among MIM's three-phase dc link, and have no influence on the overall energy balance, as (51) depicted

$$\begin{cases} \Delta P_{\text{link}a} = \frac{1}{T}\int_0^T \left(i_{ka}\cdot v_{bl}^0\right) dt = (3\sqrt{2}/4)k_{p3}I_k\Delta V_{\text{link}a} \\ \Delta P_{\text{link}b} = \frac{1}{T}\int_0^T \left(i_{kb}\cdot v_{bl}^0\right) dt = (3\sqrt{2}/4)k_{p3}I_k\Delta V_{\text{link}b} \\ \Delta P_{\text{link}c} = \frac{1}{T}\int_0^T \left(i_{kc}\cdot v_{bl}^0\right) dt = -\Delta P_{\text{link}a} - \Delta P_{\text{link}b}. \end{cases} \tag{51}$$

E. Control Strategy of MMC Part

For the control of the MMC part, the current reference values i_{od}^* and i_{oq}^* are regulated through the current inner loop. Additionally, the control block diagram of double-frequency circulating current suppression and SM capacitor voltage equalization control is shown in Fig. 12(e). Therefore, the reference values of MMC's arm voltages are shown in (52), and the MMC adopts the modulation strategy of carrier phase shift PWM

$$\begin{cases} v_{pj}^* = \frac{V_{\text{dc}}}{2} - e_j^* - u_{cirj}^* - u_{cir2j}^* - u_{cpj}^* \\ v_{nj}^* = \frac{V_{\text{dc}}}{2} + e_j^* - u_{cirj}^* - u_{cir2j}^* + u_{cnj}^*. \end{cases} \tag{52}$$

V. Topology Comparison

To further verify the advantages of eMACP-MMC, a quantitative comparison between the eMACP-MMC scheme and the existing MACP-MMC and BTB-MMC schemes will be described in the section. These three schemes are compared in terms of the adjustment range, the number of active components, semiconductor utilization (total installed die area), and the capacitance requirements.

According to the existing interconnection projects, the voltage rating of the MVac distribution network is typically 10 kV, and the MVdc distribution network is 20 kV ($\pm$10 kV). Assuming that the rated capacity of each MVac feeder is 3 MVA, the current rating is 173.21 A. The rated capacity of the MVdc feeder is 3 MW, and the current rating is 150 A.

1) For the BTB-MMC scheme, the rated capacity of an individual MMC is 3 MVA. The SM adopts a half-bridge structure. The switching device is selected as 4500 V IGBT, and the capacitor voltage is 2500 V. The number of SMs of each MMC's arm is 8.
2) For the eMACP-MMC and MACP-MMC schemes, the rated capacity is 3 MVA, and the SM also adopts a half-bridge structure. The switching devices are 4500 V IGBT, and the capacitor voltages are 2500 V. Then, 30% of the feeder voltage can be adjusted by MIM to regulate the feeders' active and reactive power. Besides, a single arm of MMC contains 8 SMs, and the rated SM's capacitor voltage is 2500 V.

A. Adjustment Range

For the BTB-MMC scheme, the active and reactive power of each feeder can be controlled independently and decoupled, enabling full-range power adjustment. For the MACP-MMC scheme, taking a single phase as an example, when the sum of the feeders' currents approaches 0, due to the insufficient balance capability of PBCM of MACP-MMC, the MIM's dc-link voltage cannot be maintained, resulting in the failed operation of MACP-MMC. For eMACP-MMC, after making a great improvement to the PBCMs' structure, the balance capability of PBCMs is greatly improved by actively injecting fundamental-frequency circulating current, thus achieving full-range adjustment.

Taking a two-feeder system as an example, the system parameters are shown in the Table II. The calculated adjustment range of MMC, MACP-MMC, and eMACP-MMC schemes are shown in Fig. 13. The results shows that eMACP-MMC compensates

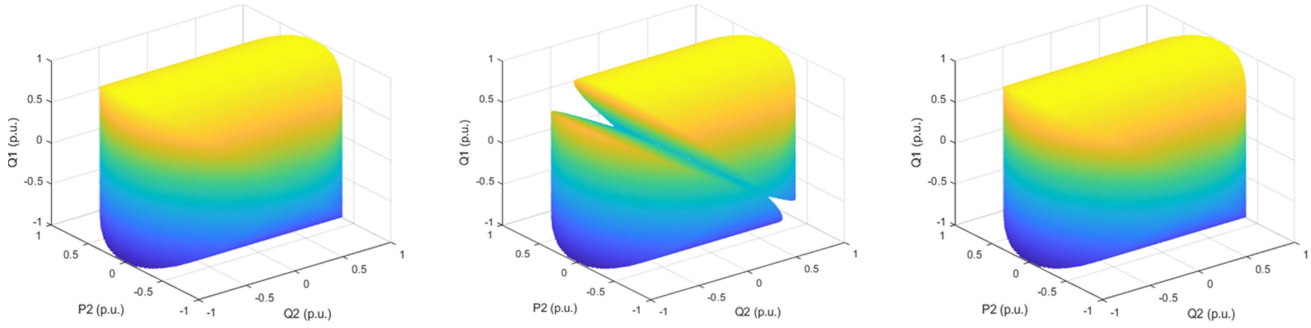

(a) BTB-MMC (b) MACP-MMC (c) eMACP-MMC

Fig. 13. Power flow adjustment range. (a) Range of BTB-MMC. (b) Range of MACP-MMC. (c) Range of MP-MMC.

TABLE II
PARAMETERS FOR CALCULATION OF ADJUSTMENT RANGE OF MACP-MMC AND EMACP-MMC

Parameter	Symbol	Value
Rated capacity of each ac feeder	S_1/S_2	1 p.u./ 1 p.u.
Rated capacity of dc feeder	S_{dc}	1 p.u.
Rated capacity of MACP-MMC	S_N	1 p.u.
Node voltage of each AC feeder	v_1/v_2	0.9 p.u./1 p.u.
Inductance of each ac feeder	L_1/L_2	0.1 p.u./ 0.1 p.u.
Reference capacitor voltage in MIM	V^*_{link}	0.3 p.u.

TABLE III
COMPONENTS OF EMACP-MMC, MACP-MMC, AND BTB-MMC

Scheme	Number of SMs in the MIM	Number of SMs in the MMC	Number of IGBTs
eMACP-MMC	3n+6	48	6n+108
MACP-MMC	3n+3	48	6n+102
BTB-MMC	0	48n	96n

for the adjustment range defects of MACP-MMC, and achieves full-range adjustment as BTB-MMC scheme.

B. Number of Active Components

A comparison of the device numbers that make up the eMACP-MMC scheme, MACP-MMC scheme and BTB-MMC scheme is shown in Table III, where n is the number of ac ports. Compared with the BTB-MMC scheme, the eMACP-MMC scheme greatly reduce the number of required electronic elements due to using a nonfull power type topology for port expansion.

C. Semiconductor Utilization

In addition to device number, semiconductor utilization is also a key factor that influences the cost, which is closely related to voltage and current ratings. As mentioned above, the voltage ratings of the semiconductors employed in these three schemes are the same. In eMACP-MMC, the current flowing through the semiconductors in the MMC and PBCMs is a superposition of the ac and dc components, the current flowing through the PFCMs' semiconductors only contains the ac component. Thus,

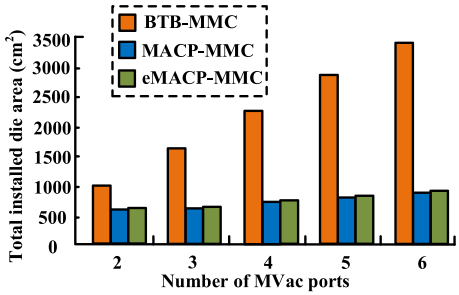

Fig. 14. Comparison of total die area installed in the BTB-MMC, MACP-MMC, and eMACP-MMC schemes.

the current ratings of semiconductors in the MIM and MMC are different. According to [23], the total estimated die area installed inside IGBT can be a comparative indicator of semiconductor utilization, which is also a measure of the minimum initial investment necessary for each topology's semiconductors. The total estimated die area installed inside Si-based IGBT packages interpolated versus nominal current rating is given in (53) for 4500 V IGBT

$$A_{\text{die}} = 3.88I + 60.23 \tag{53}$$

where A_{die} is the estimated die area, and I is the nominal current rating. The semiconductor's current rating in the PFCMs is the same as that of the MVac feeder, i.e., 173.21 A. Due to the second-order current suppression control, only the fundamental-frequency and dc components are considered when calculating the rated current of semiconductors in the MMC and PBCMs. In the supposed application scenario, the current rating of MMC's arm is 136.51 A. According to (53), the die area of semiconductors are 7.32 cm^2 in the PFCMs and 5.90 cm^2 in the PBCMs and MMC, respectively.

Considering the numbers of IGBTs shown in Table III, the total estimated die area installed in multiple MMCs, MACP-MMC, and eMACP-MMC is shown in Fig. 14. Although the die area of the individual semiconductor in MIM is larger than that of the semiconductor in MMC, the total installed die area in the eMACP-MMC is much less than the area in the BTB-MMC because the total number of IGBTs in eMACP-MMC is much fewer. From Fig. 14, the reduction of total die area is

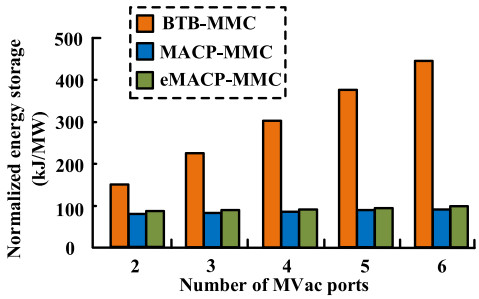

Fig. 15. Comparison of normalized energy storage in the BTB-MMC, MACP-MMC, and eMACP-MMC schemes.

more than 40% in the two ac feeders' flexible interconnection application. The benefit will be more obvious as the number of interconnecting ports increases.

D. Normalized Energy Storage

According to Siemens [24], in the case of MMC converters used for different applications, about 75% of cell volume is occupied by the capacitors installed inside of it, which significantly affect the footprint, overall power density and initial cost. The normalized energy storage (energy stored in capacitors / converter capacity) is a typically indicator, which is proportional to the device's volume. The capacitance design method of MACP-MMC is proposed in [7]. For eMACP-MMC, the capacitance value is directly related to the energy fluctuation and limited by the capacitor voltage ripple coefficient γ. Assuming that the average capacitor voltage of the MIM is controlled stably, the capacitance in the MIM (C_{MIM}) is calculated by

$$\Delta E_{\max} = \frac{nC_{\mathrm{MIM}}}{2}\left[\left(V^*_{\mathrm{link}} + \gamma V^*_{\mathrm{link}}\right)^2 - \left(V^*_{\mathrm{link}} - \gamma V^*_{\mathrm{link}}\right)^2\right]$$
$$\Rightarrow C_{\mathrm{MIM}} = \frac{\Delta E_{\max}}{2N\gamma {V^*_{\mathrm{link}}}^2}. \tag{54}$$

Consequently, the SM capacitances of the MMC and MIM in eMACP-MMC can be determined by (55) so that the voltage fluctuation can always be kept in the set range

$$\begin{cases} C_{\mathrm{MMC}} = \frac{S_N}{3\omega m N \gamma V_c^2} \\ C_{\mathrm{MIM}} = \frac{\sqrt{2}(n+1)I_N + \frac{8I_{\mathrm{dc}N}}{3}}{8\omega\cdot(n+2)\cdot\gamma V^*_{\mathrm{link}}} \end{cases} \tag{55}$$

where S_N is the apparent power of the converter, m is the voltage modulation index, N is the number of SMs per arm, n is the number of the feeders, ω is the fundamental frequency, γ is the voltage ripper of the capacitor, V_c is the rated value of the capacitor voltage in the MMC, I_N is the rated current of the ac feeder, and $V*$ link is the nominal capacitor voltage in the MIM.

The normalized energy storage can be calculated as

$$Q_N = \frac{Q_c}{S} = \frac{\frac{1}{2}C_{\mathrm{MMC\_total}}{V_{c,\mathrm{MMC}}}^2 + \frac{1}{2}C_{\mathrm{MIM\_total}}{V_{c,\mathrm{MIM}}}^2}{S}. \tag{56}$$

Fig. 15 shows a quantitative comparison of the normalized energy storage of the three schemes. The normalized energy storage, which is proportional to the device's volume, of the eMACP-MMC scheme is much lower than that of the BTB-MMC scheme. Meanwhile, the advantage will be more obvious with the increase of interconnected feeders.

In conclusion, compared with MACP-MMC scheme, BTB-MMC scheme, and eMACP-MMC scheme achieve full-range power adjustment, which is suitable for more SNOP's application scenario includes joint supply or consumption scenario and flexible interconnection scenario. Additionally, compared with BTB-MMC scheme, the eMACP-MMC solution allow for easy port expansion and have better performance regarding the number of active components, semiconductor utilization, and normalized energy storage. However, the operation principle and the control strategies of eMACP-MMC are more complicated, which are the main contributions of this article.

TABLE IV
SIMULATION PARAMETERS

Parameter	Symbol	Value
Rated capacity of ac feeder	$S_{1N}/S_{2N}/S_{3N}$	3 MVA/3 MVA/3 MVA
Rated capacity of dc feeder	S_{dcN}	3 MW
Rated capacity of the topology	S_N	3 MVA
Voltage of ac feeders (line-to-line)	$V_1/V_2/V_3$	9 kV/10 kV/10 kV
Voltage of MVdc	V_{dc}	20 kV
Inductance of each ac feeder	$L_1/L_2/L_3$	0.1 p.u./0.1 p.u. /0.1 p.u.
Carrier frequency of HBSM	$f_{s,MIM}/f_{s,MMC}$	1 kHz/1 kHz
Bridge buffer inductor of MMC	L	0.236 p.u.
Number of bridge arm SMs	N	8
SM capacitance	C_{MIM}/C_{MMC}	0.8 mF/1.6 mF
Reference capacitor voltage	$V^*_{c,MIM}/V^*_{c,MMC}$	2500 V/2500 V

TABLE V
SIMULATED CASES OF WORKING CONDITIONS

Case	P_{dc}/p.u.	Q_1/p.u.	P_2/p.u.	Q_2/p.u.	P_3/p.u.	Q_3/p.u.
1	0.75	Distributed naturally				
2	0.75	0.3	0.3	-0.2	0.3	-0.1
3	0	0.6	0.3	-0.3	-0.2	-0.3
4	-0.6	0.4	-0.2	-0.2	-0.2	-0.2

VI. SIMULATION AND EXPERIMENTAL VERIFICATION

Taking the eMACP-MMC with three ac ports as an example, this section builds a simulation model based on MATLAB/Simulink and a scale-down prototype to verify the feasibility and effectiveness of the proposed topology and the control strategy.

A. Simulation Verification

Based on the MATLAB/Simulink, a 10 kV eMACP-MMC simulation model with three ac ports is built. According to the standard IEC60038-2009, the voltage deviation of the three-phase power grid system of 1 kV–35 kV does not exceed $\pm 10\%$. Therefore, there is a voltage deviation of -10% in Feeder 1. Other parameters are shown in Table IV. The MVdc side is a dc voltage source and a resistor in series. Four different typical operating conditions are conducted to verify the effectiveness

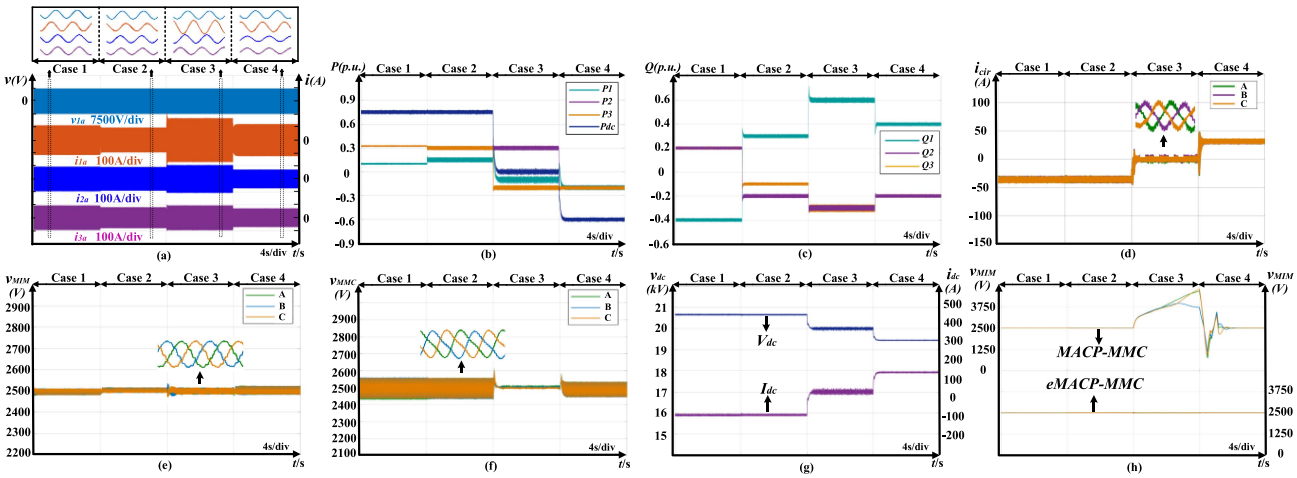

Fig. 16. Simulation results of eMACP-MMC with three 10 kV AC ports. (a) Phase-a node voltage waveform of feeder 1 and the phase-a current waveforms of three feeders. (b) Active power waveform of each feeder. (c) Reactive power waveform of each AC feeder. (d) Circulating current of MMC. (e) HBSM capacitor voltage waveform of the MIM. (f) HBSM capacitor voltage waveform of the MMC. (g) MVdc voltage and current waveforms. (h) Contrast of the HBSM capacitor voltage waveform of the MIM between eMACP-MMC and MACP-MMC.

and flexibility of eMACP-MMC, as shown in Table V, which are as follows.

1) *Case 1 (0 s–2 s):* The power of MVdc is 0.75 p.u. Without operation of the power control, the power of each feeder is naturally distributed.
2) *Case 2 (2 s–4 s):* The power of MVdc is 0.75 p.u. The power control is activated so that the active power and reactive power of the feeder are under control.
3) *Case 3 (4 s–6 s):* The power of MVdc is 0. The sum of the active power and reactive power of the feeders is 0, respectively, which is a typical condition to verify that eMACP-MMC has full-range adjustment capability compared with MACP-MMC.
4) *Case 4 (6 s–8 s):* The power of MVdc is reversed to −0.6 p.u. The active power of the feeder is reversed and evenly distributed, and the reactive power is under control.

The simulation results with three 10 kV ac ports are shown in Fig. 16. Fig. 16(a) displays the voltage and current waveforms of the ac feeders, while Fig. 16(b) and (c) shows the active and reactive power, which illustrate that the simulation achieves decoupling control of the active and reactive power with satisfactory waveform quality of the currents. Fig. 16(d) shows the three-phase circulating current waveforms of the MMC, which matches the theoretical analysis and operates within the allowable range. Fig. 16(e) and (f) presents the waveforms of the MIM's three-phase dc-link voltages and the three-phase capacitor voltages of MMC's SMs, respectively. Consequently, energy balance of the eMACP-MMC is achieved in the simulation. Additionally, Fig. 16(h) demonstrates the voltage and current waveforms of MVdc side with stable and normal operating. Finally, Fig. 16(h) compares the operation capability of MACP-MMC and eMACP-MMC: In case 3, MACP-MMC cannot maintain the capacitor voltages of MIM's dc link, while eMACP-MMC has a satisfactory operation condition. Therefore, the full-range operation capability of eMACP-MMC is verified.

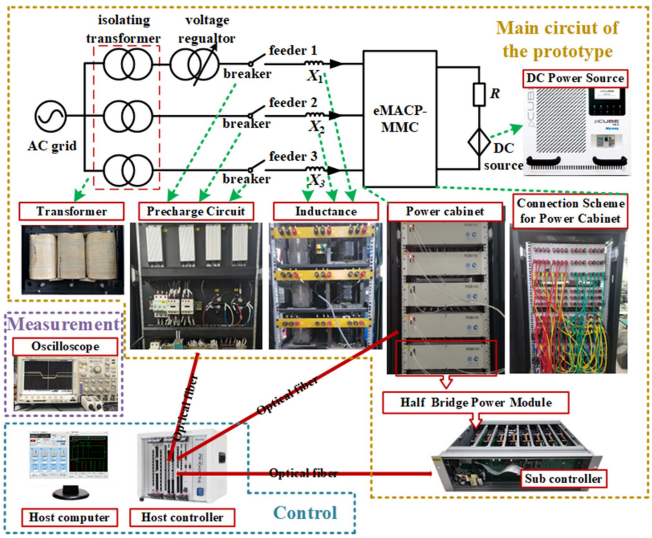

Fig. 17. System configuration diagram.

B. Experimental Verification

To further verify the feasibility and effectiveness of the proposed topology, a scale-down prototype with a capacity of 3 kVA is built for experimental verification. The prototype and its equivalent circuit are shown in Fig. 17, where the device contains a host controller, which operates the control strategy shown in Fig. 12. The subcontroller of each power module is responsible for modulation, status monitoring, and SM capacitor voltage sampling. The optical fiber is used for communication among the controllers and between the controllers and the sampling module. The experimental parameters and conditions are shown in Table VI.

The experimental results are shown in Fig. 18. Fig. 18(a) shows the overall waveform of phase-a voltage of Feeder 1

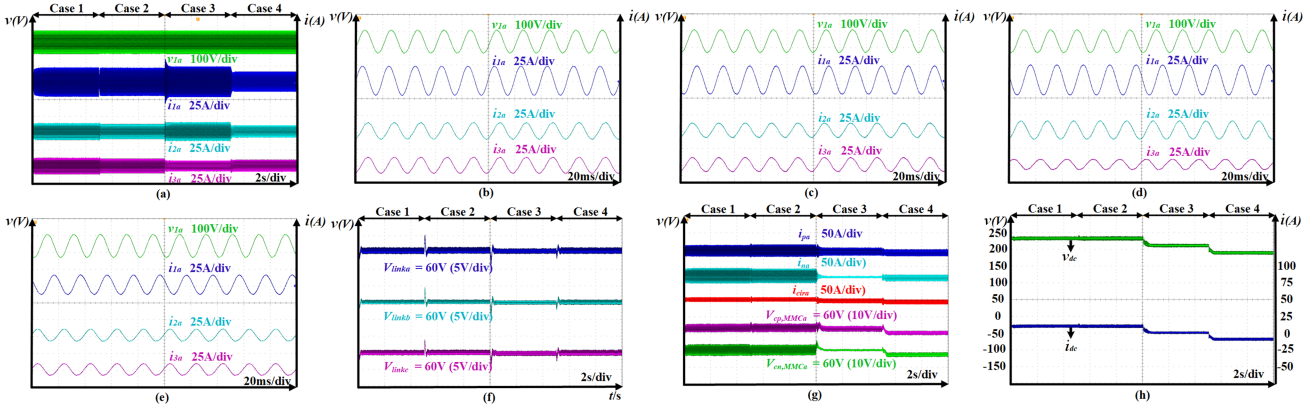

Fig. 18. Experimental results of eMACP-MMC. (a) Node voltage waveform of feeder 1 and the current waveforms of three feeders (phase-a). (b) Expanded result of case 1. (c) Expanded result of case 2. (d) Expanded result of case 3. (e) Expanded result of case 4. (f) Capacitor voltage waveforms of MIM. (g) Current and SMs' capacitor voltage waveforms of MMC's upper and lower arms and the calculated circulating current waveform. (h) Voltage and current waveforms of MVdc.

TABLE VI
EXPERIMENTAL PARAMETERS

Parameter	Symbol	Value
Rated capacity of ac feeder	$S_{1N}/S_{2N}/S_{3N}$	3 kVA/3 kVA/3 kVA
Rated capacity of dc feeder	S_{dcN}	3 kW
Voltage of ac feeder (line-to-line)	$V_1/V_2/V_3$	72 V/80 V/80 V
Voltage of MVdc	V_{dc}	240 V
Inductance of each ac feeder	$L_1/L_2/L_3$	0.295 p.u./ 0.295 p.u. /0.295 p.u.
Carrier frequency of HBSM	$f_{s,MIM}/f_{s,MMC}$	3 kHz/3 kHz
Bridge buffer inductor of MMC	L	0.295 p.u.
Number of bridge arm SMs	N	4
SM capacitance	C_{MIM}/C_{MMC}	10.8 mF/10.8 mF
Reference capacitor voltage	$V^*_{c,MIM}/V^*_{c,MMC}$	60 V/60 V

TABLE VII
EXPERIMENTAL CASES OF WORKING CONDITIONS

Case	P_{dc}/p.u.	Q_1/p.u.	P_2/p.u.	Q_2/p.u.	P_3/p.u.	Q_3/p.u.
1	0.75	Distributed naturally				
2	0.75	0.3	0.3	-0.15	0.3	-0.15
3	0	0.6	0.3	-0.3	-0.2	-0.3
4	-0.6	0.4	-0.2	-0.2	-0.2	-0.2

and currents of the three feeders. Fig. 18(b)–(e) shows the detailed current waveforms under various working conditions. The currents of feeders achieve accurate and rapid regulation, which verifies the effectiveness and feasibility of the power flow regulation control. Especially for case 3, eMACP-MMC realizes the operation under the condition that MACP-MMC cannot operate, which further verifies its full-range adjustment ability; Fig. 18(f)–(g) shows that the waveforms of MIM's dc-link capacitor voltages and MMC's capacitor voltages are stable, respectively, which verifies the feasibility of the energy balance control strategy based on fundamental-frequency circulating current injection. Fig. 18(g) also shows the current of the upper and lower arms of MMC and the circulating current waveform. The amplitude of circulating current is consistent with the theoretical calculation and is acceptable. Fig. 18(h) shows that the voltage and current waveforms of MVdc are in the normal operating range.

VII. CONCLUSION

This article presents a novel multiport SNOP topology called eMACP-MMC, which realizes full-range adjustment, which is suitable for not only the joint supply or consumption scenario as MACP-MMC but also the flexible interconnection scenario where the power is regulated among the ac feeders. The main contributions can be concluded as follows.

1) The internal energy balance mechanism of eMACP-MMC's MIM based on actively injecting circulating current is proposed. Meanwhile, the circulating current's other control degree of freedom is used to eliminate the imbalance between the MMC's arms caused by the former component. Meanwhile, the corresponding control strategies are designed.
2) Considering the shortcomings caused by the circulating current, the redundant degree of freedom can be used to optimize the system operation with the principle of minimizing the injected circulating current from two aspects.
3) A quantitative comparison between the eMACP-MMC scheme and the existing schemes of MACP-MMC and BTB-MMC is conducted to further verify the advantages of eMACP-MMC in cost, volume, and operating range.
4) Simulation and experimental results further validate the effectiveness of the proposed topology and its control strategies.

REFERENCES

[1] J. Zhang, Y. Zhang, J. Zhou, J. Wang, G. Shi, and X. Cai, "Control of a hybrid modular solid-state transformer for uninterrupted power supply under MVdc short-circuit fault," *IEEE Trans. Ind. Electron.*, vol. 70, no. 1, pp. 76–87, Jan. 2023.

[2] J. M. Bloemink and T. C. Green, "Increasing distributed generation penetration using soft normally-open points," in *Proc. IEEE PES Gen. Meeting*, Minneapolis, MN, USA, 2010, pp. 1–8.

[3] Y. Chen, J. Sun, X. Zha, Y. Yang, and F. Xu, "A novel node flexibility evaluation method of active distribution network for SNOP integration," *IEEE J. Emerg. Sel. Topics Circuits Syst.*, vol. 11, no. 1, pp. 188–198, Mar. 2021.
[4] F. Katiraei and J. R. Agüero, "Solar PV integration challenges," *IEEE Power Energy Mag.*, vol. 9, no. 3, pp. 62–71, May/Jun. 2011.
[5] L. Zhang, C. Wang, J. Liang, M. Wu, B. Zhang, and W. Tang, "A coordinated restoration method of hybrid AC/DC distribution network for resilience enhancement," *IEEE Trans. Smart Grid*, vol. 14, no. 1, pp. 112–125, Jan. 2023.
[6] J. Pereda and T. C. Green, "Direct modular multilevel converter with six branches for flexible distribution networks," *IEEE Trans. Power Del.*, vol. 31, no. 4, pp. 1728–1737, Aug. 2016.
[7] D. Karwatzki and A. Mertens, "Generalized control approach for a class of modular multilevel converter topologies," *IEEE Trans. Power Electron.*, vol. 33, no. 4, pp. 2888–2900, Apr. 2018.
[8] H. Peng, J. Zhang, J. Zhou, G. Shi, J. Wang, and X. Cai, "Delta-type serial shunt soft normally-open points with wide power flow regulation range in distributed network," *IEEE Trans. Ind. Electron.*, vol. 71, no. 7, pp. 6501–6511, Jul. 2024.
[9] S. Kolluri, N. B. Y. Gorla, and S. K. Panda, "Capacitor voltage ripple suppression in a modular multilevel converter using frequency-adaptive spatial repetitive-based circulating current controller," *IEEE Trans. Power Electron.*, vol. 35, no. 9, pp. 9839–9849, Sep. 2020.
[10] D. Samajdar and T. Bhattacharya, "Capacitor voltage ripple optimization in modular multilevel converter using synchronous reference frame energy ripple controller," *IEEE Trans. Power Electron.*, vol. 37, no. 7, pp. 7883–7895, Jul. 2022.
[11] T. Younis, P. Mattavelli, I. Toigo, and M. Corradin, "Circulating current control for a three-phase modified modular multilevel converter with a reduced number of current sensors," *IEEE Trans. Ind. Appl.*, vol. 59, no. 4, pp. 4409–4417, Jul./Aug. 2023.
[12] B. Li, Y. Zhang, G. Wang, W. Sun, D. Xu, and W. Wang, "A modified modular multilevel converter with reduced capacitor voltage fluctuation," *IEEE Trans. Ind. Electron.*, vol. 62, no. 10, pp. 6108–6119, Oct. 2015.
[13] M. Huang, Z. Kang, W. Li, J. Zou, X. Ma, and J. Li, "Modified modular multilevel converter with third-order harmonic voltage injection to reduce submodule capacitor voltage ripples," *IEEE Trans. Power Electron.*, vol. 36, no. 6, pp. 7074–7086, Jun. 2021.
[14] G. Jia, M. Chen, S. Tang, C. Zhang, and G. Zhu, "Active power decoupling for a modified modular multilevel converter to decrease submodule capacitor voltage ripples and power losses," *IEEE Trans. Power Electron.*, vol. 36, no. 3, pp. 2835–2851, Mar. 2021.
[15] D. D. Le and D.-C. Lee, "A modular multilevel converter topology with novel middle submodules to reduce capacitor voltage fluctuations," *IEEE Trans. Power Electron.*, vol. 37, no. 1, pp. 70–75, Jan. 2022.
[16] G. Jia, B. Shi, M. Li, M. Chen, F. Niu, and Y. Tang, "Active power decoupling for full-bridge submodules of a modular multilevel converter," *IEEE Trans. Power Electron.*, vol. 39, no. 8, pp. 9752–9764, Aug. 2024.
[17] J. Zhang et al., "A modular multilevel converter station with multiple MVac ports," *IEEE Trans. Ind. Electron.*, vol. 70, no. 9, pp. 8655–8665, Sep. 2023.
[18] J. Zhang et al., "Series–shunt multiport soft normally open points," *IEEE Trans. Ind. Electron.*, vol. 70, no. 11, pp. 10811–10821, Nov. 2023.
[19] Y.-N. Jang and J.-W. Park, "New circulating current suppression control for MMC without arm current sensors," *IEEE Trans. Power Electron.*, vol. 39, no. 9, pp. 11232–11243, Sep. 2024.
[20] J. zhou, J. Zhang, G. Shi, and X. Cai, "Exploration on power converter topologies applied in flexible interconnection of distribution system," *Proc. CSEE*, vol. 39, no. 1, pp. 277–288, Jan. 2019.
[21] B. C. Kuo and F. Golnaraghi, "Frequency-domain analysis," in *Automatic Control System*, 8th ed. New York, NY, USA: Wiley, 2003, pp. 352–421.
[22] D. Lu, J. Zhu, J. Wang, J. Yao, S. Wang, and H. Hu, "A simple zero-sequence-voltage-based cluster voltage balancing control and the negative sequence current compensation region identification for star-connected cascaded H-bridge STATCOM," *IEEE Trans. Power Electron.*, vol. 33, no. 10, pp. 8376–8387, Oct. 2018.
[23] A. Marzoughi, R. Burgos, D. Boroyevich, and Y. Xue, "Design and comparison of cascaded H-bridge, modular multilevel converter, and 5-L active neutral point clamped topologies for motor drive applications," *IEEE Trans. Ind. Appl.*, vol. 54, no. 2, pp. 1404–1413, Mar./Apr. 2018.
[24] M. A. Perez, S. Bernet, J. Rodriguez, S. Kouro, and R. Lizana, "Circuit topologies, modeling, control schemes, and applications of modular multilevel converters," *IEEE Trans. Power Electron.*, vol. 30, no. 1, pp. 4–17, Jan. 2015.

Junxian Chen received the B.S. degree in electrical engineering, in 2023 from Shanghai Jiao Tong University, Shanghai, China, where he is currently working toward the M.S. degree in electrical engineering with the School of Electronics Information and Electrical Engineering.

His research interests include ac–dc hybrid distribution network, multiport converter, and multilevel converter.

Jianwen Zhang (Senior Member, IEEE) received the B.Eng., M.Sc., and Ph.D. degrees in electrical engineering from Shanghai Jiao Tong University, Shanghai, China, in 2003, 2006, and 2014, respectively.

He is currently a Professor with Shanghai Jiao Tong University. His current research interests include topology, operation, and control of power conversion systems.

Jianqiao Zhou (Member, IEEE) received the B.Sc. degree in electric engineering from Xi'an Jiao Tong University, Xi'an, China, in 2014, and the Ph.D. degree in electrical engineering from Shanghai Jiao Tong University, Shanghai, China, in 2020.

He is currently an Assistant Professor with the Wind Power Research Center, Shanghai Jiao Tong University. His current research interests include solid-state transformers and multiport converters.

Gang Shi (Member, IEEE) received the B.Eng., M.Sc., and Ph.D. degrees in electrical engineering from Shanghai Jiao Tong University, Shanghai, China, in 2007, 2009, and 2014, respectively.

He was as a Research Fellow with the School of Electronic Electrical and Systems Engineering, University of Birmingham, U.K., from 2017 to 2018. He is currently an Associate Professor with the Wind Power Research Center, Shanghai Jiao Tong University. His current research interests include operation and control of hybrid ac–dc grid.

Yajun Jia received the master's degree in electrical engineering in 2004 from Shanghai Jiao Tong University, Shanghai, China, where since 2020, he has been working toward the Ph.D. degree in electrical engineering.

From 2012 to 2021, he was a Full-Time Researcher with the National Energy Smart Grid (Shanghai) R&D Center. His current research interests include fault diagnosis in distribution networks, equipment status monitoring, and operation and control of power conversion system.

Han Wang received the B.Sc. degree from China University of Mining and Technology, Beijing, China, in 2005, the M.Sc. and Ph.D. degrees from Shanghai Jiao Tong University, Shanghai, China, in 2008 and 2013, respectively, all in electrical engineering.

During 2014–2019, he was an Engineer with Shanghai Mitsubishi Elevator Company, Shanghai Electric Group. During 2019–2021, he was a Postdoctoral Research Fellow with the Department of Electrical Engineering, Shanghai Jiao Tong University. Since 2019, he has been a Research Assistant with the Department of Electrical Engineering, Shanghai Jiao Tong University. His research interests include high power converters, renewable energy generation, and grid integration.

Xu Cai (Senior Member, IEEE) received the B.Eng. degree from Southeast University, Nanjing, China, in 1983, and the M.Sc. and Ph.D. degrees from the China University of Mining and Technology, Xuzhou, China, in 1988 and 2000, respectively, all in electrical engineering.

In 2002, he was a Professor with Shanghai Jiao Tong University, Shanghai, China, where he has been the Director of Wind Power Research Center, since 2008. His research interests include power electronics and renewable energy exploitation and utilization.